

Performance Optimization of Plate Airfoils for Martian Rotor Applications Using a Genetic Algorithm

Witold J. F. Koning
Aerospace Engineer
 Science and Technology Corporation
 NASA Ames Research Center
 Moffett Field, California

Ethan A. Romander
Aerospace Engineer
 NASA Ames Research Center
 Moffett Field, California

Wayne Johnson
Aerospace Engineer

ABSTRACT

The Mars Helicopter Technology Demonstrator will be flying on the NASA Mars 2020 rover mission scheduled to launch in July of 2020. The goal is to demonstrate the viability and potential of heavier-than-air vehicles in the Martian atmosphere. Research is performed at the Jet Propulsion Laboratory and NASA Ames Research Center to extend these capabilities and develop the Mars Science Helicopter as the next possible step for Martian rotorcraft. The Mars Science Helicopter mass is scaled up to the 5 to 20 kg range, allowing a greater payload (approximately 0.5 to 2.0 kg), and greater range (approximately 3 km). Key to achieving these targets is careful aerodynamic rotor design. The Martian atmosphere's low density and the small helicopter rotors result in very low chord-based Reynolds number flows, which reduces rotor performance. A continuous genetic algorithm is developed to optimize airfoil shapes at representative conditions for the Martian atmosphere. Previous research indicates that sharp leading edges and plate-like airfoils can out-perform conventional airfoil shapes. The present optimization allows for camber and thickness variation of curved and polygonal thin airfoils with sharp leading edges. The airfoil performance is evaluated at the highest attainable lift-to-drag ratio near a moderate lift coefficient at compressible Mach numbers, as expected for Martian rotor application. Increases between 16% and 29% in airfoil lift-to-drag ratio at fixed lift coefficients are observed when compared with the Mars Helicopter Technology Demonstrator airfoils. Improvements in hover figure of merit are estimated to be between 4% and 10%, when applied to the Mars Helicopter Technology Demonstrator.

NOTATION

B	point on Bézier curve (vector)	T	absolute temperature
c	airfoil chord	x_1, x_2	test function variables
c_d	section drag coefficient	y^+	dimensionless wall distance
c_l	section lift coefficient	α	angle of attack
c_{l*}	target section lift coefficient	γ	specific heat ratio
$c_{l,tolerance}$	allowed deviation from target lift coefficient	μ	dynamic viscosity
c_m	section moment coefficient	ρ	density
f	airfoil camber	τ	Bézier interval
F	fitness function	ACA	Arbitrary Continuous Airfoil
M	Mach number	AFT	Amplification Factor Transport
P_i	control point i of Bézier curve (vector)	BDF2	Backward Difference Formula (2 nd order)
r	rotor radial coordinate	CFD	Computational Fluid Dynamics
R	gas constant; rotor radius	CGA	Continuous Genetic Algorithm
Re	Reynolds number	CGT	Chimera Grid Tools
Re_c	chord-based Reynolds number	CO2	Carbon Dioxide
t	airfoil thickness	CP	Cambered Plate
t_b	baseline thickness		

Presented at the 45th European Rotorcraft Forum, Warsaw, Poland, 17-20 September, 2019.

Used with permission. © 2019 National Aeronautics and Space Administration.

The Work is co-authored by NASA employees and a non-U.S. Government author. U.S. copyright protection does not attach to separable portions of a Work authored solely by U.S. Government employees as part of their official duties. The U.S. Government is the owner of foreign copyrights in such separable portions of the Work and is a joint owner (with the non- U.S. Government author) of U.S. and foreign copyrights that may be asserted in inseparable portions of the Work. The U.S. Government retains the right to use, reproduce, distribute, create derivative works, perform and display portions of the Work authored solely or co-authored by a U.S. Government employee. The authors confirm that they, and/or their company or organization, hold copyright on all of the original material included in this paper. The authors also confirm that they have obtained permission, from the copyright holder of any third party material included in this paper, to publish it as part of their paper. The authors confirm that they give permission, or have obtained permission from the copyright holder of this paper, for the publication and distribution of this paper as part of the ERF proceedings or as individual offprints from the proceedings and for inclusion in a freely accessible web-based repository.

DEP	Double-Edged Plate
DNS	Direct Numerical Simulation
FFT	Fast Fourier Transform
GA	Genetic Algorithm
HALE	High-Altitude Long Endurance
JPL	Jet Propulsion Laboratory
KH	Kelvin-Helmholtz
LDS	Low Discrepancy Sequence
LE	Leading Edge
MAV	Micro Aerial Vehicle
MHTD	Mars Helicopter Technology Demonstrator
MOO	Multi Objective Optimization
MSH	Mars Science Helicopter
PARSEC	Airfoil Parameterization Method
PAT	Polygonal Airfoil
RANS	Reynolds-Averaged Navier-Stokes
SA	Spalart-Allmaras
SLS	Sea Level Standard
SOO	Singe Objective Optimization
TE	Trailing Edge
UAV	Unmanned Aerial Vehicle

INTRODUCTION

The Mars Helicopter Technology Demonstrator (MHTD) will be flying on the NASA Mars 2020 rover mission. The Martian atmosphere’s low density and the helicopter’s relatively small rotor result in very low chord-based Reynolds number flows, around $Re_c = O(10^3-10^4)$. This reduces the rotor lifting force and efficiency, which is only partially compensated for by a lower gravity on Mars compared to that of Earth. Additionally, the low temperature and largely CO₂ based atmosphere of Mars compound the overall aerodynamic problem by resulting in a lower speed of sound, further constraining rotor operation in the Martian atmosphere by limiting the maximum rotor tip speed possible so as not to exceed an acceptable tip Mach number.

In light of the expected reduced rotor efficiency, evaluation of airfoils for compressible, low-Reynolds number environments is key. Prior research on airfoil optimization and performance evaluation at low Reynolds numbers, especially in the compressible regime, is scarce and requires further understanding. Specifically, the proposed goal stemming from this paper is to explore airfoils tailored to the unique demands of the second generation of Mars rotorcraft; the Mars Science Helicopter (MSH).¹

Research is performed at the Jet Propulsion Laboratory (JPL) and NASA Ames Research Center to extend the capabilities and develop the MSH as the next possible step for Martian rotorcraft. The MSH mass is scaled up to the 5 to 20 kg range, allowing for a science payload (approximately 0.5 to 2.0 kg), and greater range (from 900 m to approximately 3000 m).^{1,2} Key to achieving these targets is careful aerodynamic design of the rotor. Results from this investigation at the lower Mach range are applicable to rotors for Micro

Aerial Vehicles (MAV) and small Unmanned Aerial Vehicles (UAV) on Earth, High-Altitude Long Endurance (HALE) aircraft, as well as UAVs in the Martian atmosphere.

Prior research found the cambered plate airfoil in this regime to out-perform conventional airfoils,³ but the geometry variation for cambered plates in literature is limited,⁴⁻⁹ implying airfoil performance optimization for plates (wherein nonlinear camber lines, chordwise plate thickness distributions, and even local corrugation features can be examined)¹⁰ could yield performance improvements over the ‘simple cambered plate’ often presented in literature. A continuous genetic algorithm (CGA) is developed following the approach by Holst and Pulliam for conventional airfoil optimization.¹¹ The present optimization allows for camber and thickness variation in curved and polygonal thin airfoils with sharp leading edges. Structured grids for Computational Fluid Dynamics (CFD) analyses are automatically generated. This approach will allow airfoil optimization of camber, thickness, and leading edge shape distributions and will evaluate smooth versus sharp edges along the airfoil surface.

The complexity of the flow features for a plate airfoil at low Reynolds numbers requires (at least^{12,13}) the use of a Reynolds-Averaged Navier-Stokes (RANS) solution for the flow field using a turbulence transition method. The airfoil performance will be evaluated as the highest attainable lift-to-drag ratio near a moderate lift coefficient at compressible Mach numbers, as expected for a Martian rotor application.¹⁴

This research focuses on airfoil performance at low Reynolds numbers and hopes to add to the work performed by Kroo et al.,¹⁵ Kunz and Kroo,¹⁶ Oyama and Fujii,¹⁷ Anyoji et al.,¹⁸⁻²⁰ Winslow et al.,²¹ amongst others. Optimization of airfoils in this regime is scarce but has been performed by Srinath and Mittal²² and Désert, Moschetta, and Bézard.²³

MARS HELICOPTER

Figure 1 shows the Flight Model of the MHTD inside the Space Simulator at JPL.



Figure 1 Members of the NASA Mars Helicopter team attach a thermal film to the exterior of the flight model of the Mars Helicopter.²⁴

The MHTD will be flying on the Mars 2020 mission to demonstrate the viability and potential of heavier-than-air vehicles in the Martian atmosphere. The MHTD features a co-axial rotor design with two counter-rotating, hingeless, two-bladed rotors. Figure 2 shows a close-up of the flight model’s hub. The rotors are spaced apart at approximately 8% of the rotor diameter and are designed to operate at speeds up to 2,800 RPM. The vehicle has a mass of roughly 1.8 kg and rotor diameter of 1.21 m. The helicopter relies on solar cells and a battery system for power, allowing up to 90 second flight endurance that is conducted fully autonomously due to the communication delay between Earth and Mars. Flights are limited to favorable weather with low wind and gust speeds. The maximum airspeed is constrained to 10 m/s horizontally and 3 m/s vertically.

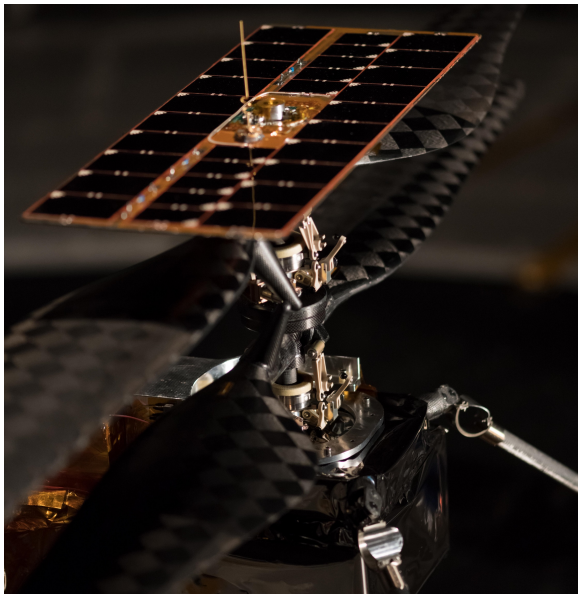


Figure 2 Close-up of the hub, solar panel, and inboard rotor of the MHTD Flight Model.²⁴

Balaram et al. describe the MHTD and its key features,²⁵ Grip et al. describe the flight dynamics,²⁶ and Grip et al. discuss the guidance and control for the helicopter.²⁷ Pipenberg et al. describe the fabrication of the MHTD.²⁸ Rotor performance analyses on the Mars Helicopter are performed by Koning, Johnson, and Grip to predict the MHTD rotor performance and compare to experimental testing in the JPL Space Simulator at Martian atmospheric densities.²⁹

The MSH concept is designed to extend these capabilities, allowing a greater payload (approximately 0.5 to 2.0 kg), and greater range (approximately 3000 m).^{1,2} Amidst many technological advances that can make this vehicle a reality, key to achieving these targets is careful aerodynamic design of the rotor.

LOW REYNOLDS NUMBER AERODYNAMICS

A brief overview of low Reynolds number aerodynamics, subcritical airfoil performance, laminar separation bubbles, free shear layer instability, flow structures, and cambered plate performance is presented in Koning et al.²⁹ and Koning.¹⁰ For the benefit of the reader, some parts are repeated here.

At the Reynolds number range under consideration, $Re_c = O(10^3-10^4)$, the boundary layer can be fully laminar up to the point of separation without subsequent (turbulent) flow reattachment or on-body transition. The flow state in absence of laminar-to-turbulent transition is called subcritical and derives its relatively low efficiency due to: (a) the increased pressure drag component from early separation and, to lesser extent, (b) reduced lift due to an effective camber reduction.

The Reynolds number at which laminar flow over an airfoil begins to exhibit turbulent features (either due to on-body transition or turbulent reattachment) is called the critical Reynolds number. Reynolds numbers where turbulent transition always occurs before laminar separation or during/after reattachment are referred to as supercritical. Compressible flow is not well understood for low-Reynolds number airfoils. Limited experimental and computational work in the literature^{18-20,30} – and performed previously by the authors³ – would suggest that conventional airfoil geometries exhibit Mach-number sensitivities whereas cambered, flat-plate airfoils seem to be insensitive to Mach number.^{18,20}

The ‘transitional region’ between the two flow states (sub- and supercritical) is difficult to analyze and reliably predict⁴ due to the possible contribution of external influences such as freestream turbulence levels, vibrations, and surface roughness on boundary layer and separated shear layer stability with subsequent laminar-turbulent transition.^{5,31} Besides possible hysteresis,⁴ unsteady laminar separation (bubble) features, shedding of vortices, and transient boundary layer transition behavior can give rise to unpredictable flight dynamics.⁷ The receptivity (the process by which free-stream disturbances influence or generate instabilities in the boundary layer) and the source of initial disturbances leading to laminar-turbulent transition is discussed by Saric, Reed, and Kerschen.³²

SHARP LEADING EDGE AERODYNAMICS

In contrast to a regular airfoil, cambered plate performance has been shown to be almost Reynolds number independent.⁴ The Reynolds number independence is mostly attributed to a sharp leading edge, fixing the separation location in contrast to the

variable separation point of regular airfoils. Prior research found the cambered plate in this regime potentially out-performs conventional airfoils (in terms of minimum drag, maximum lift-to-drag ratio, and possibly maximum lift coefficient,) ^{4-7,33-35} but the geometry variation for cambered plates in references is limited. ⁴⁻⁹ Previous work also indicates the competitiveness of cambered plates versus airfoils for rotor performance for the MHTD. ^{3,29}

Despite the Reynolds number independence, (cambered) plate performance analysis is difficult due to the flow instability after leading-edge separation, possibly leading to separation bubbles. The stability characteristics of the separated (free) shear layers are fundamentally different from the (attached) boundary layer. ³² Laminar-turbulent transition of the flow in the separated shear layer can occur, and the possible subsequent re-attachment of the boundary layer further increases the complexity of the flow physics. Schmitz ⁴ lists the ‘*advantageous cooperation of tangential incident flow at the leading edge at large angles of attack with the turbulence effect of the small nose radius,*’ as one of the reasons for the competitive performance of the cambered plate at low Reynolds numbers. The laminar separation bubble is often only described as ‘reattaching due to transition to turbulence’. When the Reynolds number is sufficiently reduced, the separated shear layer might still reattach even if the sharp leading edge does not cause the separated shear layer to transition. This laminar reattachment is observed in experiments for a flat plate around $Re_c = 10,000$. ^{36,37}

Vortex shedding is observed in particular behind sharp edges and near large variations in pressure gradient. ^{3,5,38} The origin of the coherent vortices might be a ‘shedding’-type instability or separated shear layer disturbance growth following linear stability mechanisms. ³⁸ In addition, Kelvin-Helmholtz (KH) instabilities (and subsequent KH vortices) can alter the separated shear layer behavior. ³⁹ The commonly used term ‘bubble bursting’ might in fact be time-averaged periodic shedding of vortices, ⁴⁰ and therefore not yet lead to a complete stall of the airfoil with which it is sometimes correlated. Laminar-turbulent transition might play only a minor role compared to coherent vortices shed into the reattached boundary layer that dominate the separation region. ³⁸

CONTINUOUS GENETIC ALGORITHM

The optimization strategy employs a continuous genetic algorithm (CGA). A genetic algorithm (GA) is a type of evolutionary computation, first developed by Holland, ⁴¹ that allows for a natural exploration of the solution space. In the present work, it is used to provide

insight into the performance of two-dimensional performance of various airfoil shapes. Holland and Goldberg ⁴² describe genetic algorithms as ‘*search algorithms based on the mechanics of natural selection and natural genetics.*’ Through various genetic operators such as recombination, selection, and mutation, the algorithm can maximize an arbitrary fitness function (or minimize a cost function). The CGA starts with a random initial population of *chromosomes*. Each chromosome contains a series of *genes* with each gene encoding a single design parameter. The algorithm applies the genetic operators to these chromosomes to obtain the subsequent generation. This process is repeated until a convergence criterion is met based on the fitness function evaluation.

The choice for a GA was made based primarily on its robustness and ability to explore a solution space without too much concern for continuity, derivatives, or unimodality (the existence of only one optimum) of the search space. The genetic algorithm approach and parameters for airfoil optimization as described by Holst and Pulliam ¹¹ are closely followed for the present optimization. Efficient shapes for the airfoils under consideration are mostly unexplored to date, making a GA a good candidate.

The main tradeoff made is exploration versus exploitation. A calculus-based optimization method can quickly find the maximum of a continuous, unimodal function (exploitation), but it struggles when presented with many local optima. The GA allows for many small subpopulations to explore local extremes in the global design space, at the cost of reduced efficiency. ⁴³ Performance optimization for plate type airfoils can yield a solution space with various local minima, making gradient-based optimization techniques less appealing due to the necessity of finding a good starting location.

Airfoil optimization using genetic algorithms has been used in the past, often using a number of control points connected with splines ^{17,22,44-46} and/or the PARSEC method ^{47,48} specifically designed for airfoil parameterization. ^{11,49} An approach using many control points is not desired as each of those will increase the budget for convergence. With the function evaluations being relatively expensive RANS cases, the number of control points needs to be kept small.

The goal of this paper is not to present a highly-efficient GA for general airfoil optimization. In effect, with different aerodynamic regimes under consideration, the optimal GA likely differs. Since the objective function uses a CFD solver, not much is known a priori about the solution space, and hence, designing an ‘optimal’ GA would only be marginally useful since it would be specific to the problem at hand.

GENETIC ALGORITHM PARAMETERS

The optimization parameters are described in Table 1. The initialization of the population is chosen at random within constraints, depending on the airfoil type. As randomization does not avoid accidental clustering of points, tests were performed with low discrepancy sequences (LDS) to spread out the initial population. However, the marginal gain was not deemed valuable in light of the extra effort required to properly apply the LDS to initialization whilst respecting the airfoil constraints.

Holst and Pulliam¹¹ use a form of fitness proportionate selection. Selection is performed by sampling (with replacement) after ranking the fitness of each chromosome. On the selected samples the following four operators are subsequently performed:

- Passthrough (or elitism) is used to keep the 10% of the chromosomes with the lowest cost function value from the previous population, ensuring that the highest fitness value can never decrease with increasing number of generations.
- Random average crossover is performed on 20% of the selection. A new chromosome is formed by averaging between the two randomly chosen chromosomes.
- Perturbation mutations are performed on 40% of the selected chromosomes, allowing one randomly chosen gene to perturb slightly, allowing for exploitation of an area within the search space that the particular chromosome resides in.
- The final 30% of the population is mutated. One gene of each chosen chromosome is randomly varied within the allowed constraints.

The parameters described above allow for a balanced exploration versus exploitation of the solution space.

Table 1 Parameters of the optimization algorithm

Parameter	Value
Initialization	Random (constrained)
Genes per chromosome	4 ~ 11 (depending on airfoil type)
Population size	20 (fixed)
Number of generations	55 ~ 180 (depending on airfoil type)
Selection	Fitness proportionate selection
Offspring generation	Non-repeating passthrough (10%), Random average cross-over (20%), Perturbation mutation (constrained, 40%), Mutation (constrained, 30%)

DESIGN SPACE

Four airfoil types were examined. Constraints were applied to ensure that practically all gene combinations yield airfoils with realizable geometry.

Cambered Plate (CP)

Previous work indicated that circular arc cambered plate airfoils are aerodynamically efficient. Curved distributions of camber or thickness are parameterized

using cubic Bézier curves. The cubic Bézier curve takes shape in the following form, shown in Equation 1.

$$\mathbf{B}(\tau) = (1 - \tau)^3 \mathbf{P}_0 + 3(1 - \tau)^2 \tau \mathbf{P}_1 + 3(1 - \tau) \tau^2 \mathbf{P}_2 + \tau^3 \mathbf{P}_3 \quad (1)$$

where τ is the Bézier interval ranging from $\tau = 0$ to $\tau = 1$, $\mathbf{P}_i = [x, y]$ are vectors containing the control points (with i ranging from $i = 0$ to $i = 3$), and $\mathbf{B}(\tau) = [x, y]$ is the point on the Bézier curve for the chosen value of the Bézier interval, τ .

The control points are constrained so that x is monotonic in τ , and correspondingly, for each x value there can only be one y value. Cubic Bézier curves can have one or two inflection points, a cusp, be a plain curve, or can contain a loop. Stone and DeRose analyze planar parametric cubic curves and determine the conditions for loops, cusps, and inflection points.⁵⁰ The approach by Stone and DeRose is used to ensure constraints enforce the absence of loops as they result in impossible airfoil geometry. Inflection points and cusps are allowed.

While a cubic Bézier curve cannot exactly represent a circular arc, the error is very small in radius, on the order of 10^{-6} .⁵¹ The maximum absolute error in nondimensional camber for the approximation of a 5% circular arc airfoil using a cubic Bézier curve is less than $4.00 \cdot 10^{-5}$.

An overview of the constraints is presented in Table 2. The buildup of the chromosome for the CP optimization is shown in Table 3.

Table 2 Cambered plate basic constraints

Constraint	Minimum	Maximum
Camber slope	-0.50	0.50
Camber height (y/c)	-0.10	0.10
Baseline thickness (t/c)	0.01	0.01

Table 3 Cambered plate chromosome buildup

Gene	Parameter
1	Camber cubic Bézier 1 st control point 1 x
2	Camber cubic Bézier 1 st control point 1 y
3	Camber cubic Bézier 2 nd control point 2 x
4	Camber cubic Bézier 2 nd control point 2 y

The CP airfoils have a fixed thickness distribution which is shown in Figure 3. The plate has a thickness of $t/c = 0.01$ to allow a structurally realistic design. The sharp leading edge blends smoothly with the constant thickness plate over the first 10% of the chord. The trailing edge is blunt with a thickness of $t/c = 0.01$.

Figure 3 shows the cubic Bézier curve representing the camber line, the airfoil thickness distribution, and the final airfoil shape.

The camber control points are visualized with the black circles and are constrained to not let the leading and trailing edge slopes exceed the constraints. The maximum slope of the curve and camber height is also constrained.

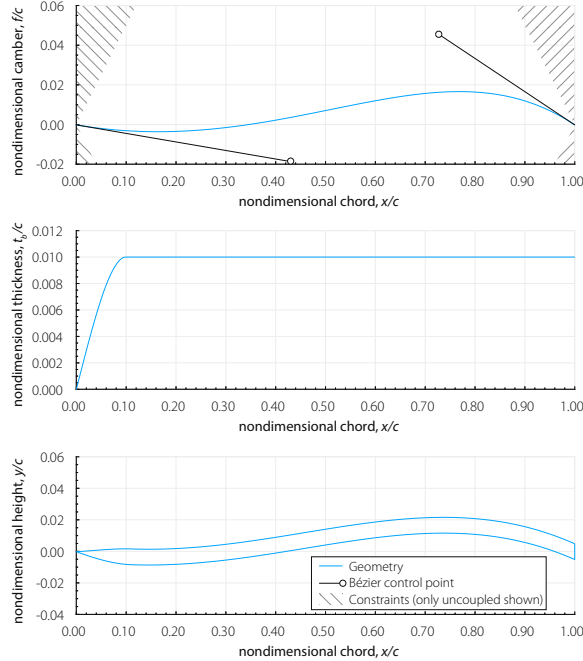


Figure 3 Cambered plate camber, baseline thickness, and airfoil shape. The vertical axis is enlarged to show details.

Arbitrary Continuous Airfoil (ACA)

An arbitrary continuous airfoil (ACA) is a profile that has sharp leading and trailing edges but is allowed to vary in both camber and thickness. The camber line is modeled identically to the camber line of the cambered plate (CP) airfoil. The thickness is varied using two cubic Bézier curves.

The first Bézier curve defines a baseline thickness that constrains the airfoil to a minimum thickness of $t/c = 0.01$ and ensures that the sharp leading and trailing edges blend smoothly with this constraint. The distance over which this blending takes place is allowed to vary and is mirrored from the leading onto the trailing edge to reduce the number of genes required.

A second Bézier curve defines a thickness increment to be added to the baseline thickness. The increment is forced to zero at the leading and trailing edges to preserve sharpness but is allowed to vary smoothly in between, subject to the constraints given in Table 4. The transition length of the baseline thickness is now also allowed to change through a cubic Bézier curve and is mirrored onto the trailing edge. This allows for modification of the sharpness of the leading and trailing edge.

Table 5 lists the genes that comprise a chromosome for an arbitrary continuous airfoil. Note that gene 6 and 8 could be zero which would result in zero thickness increment and result in a plate airfoil with sharp leading and trailing edges.

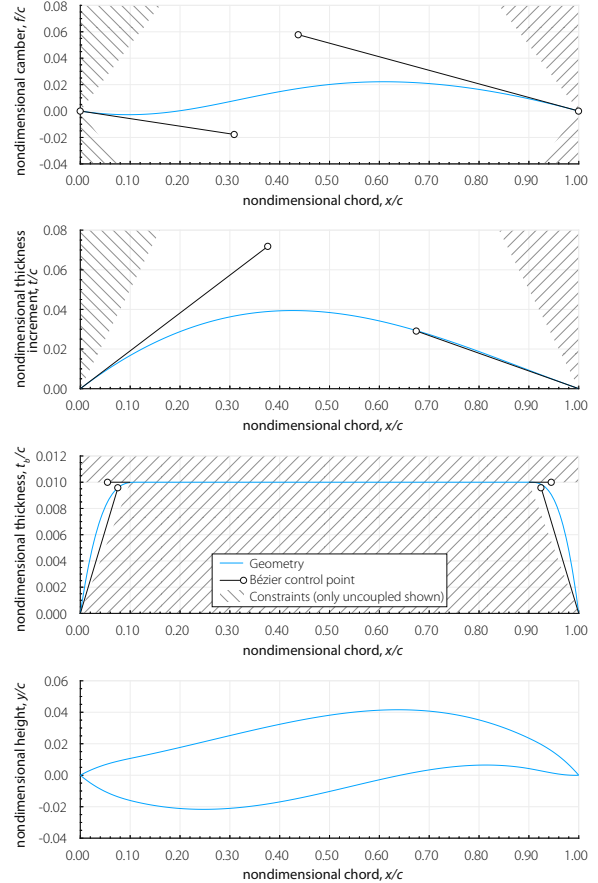


Figure 4 Arbitrary continuous airfoil camber, thickness increment, baseline thickness, and airfoil shape. The vertical axis is enlarged to show details.

The ACA optimization might allow for higher performance airfoils (any optimum from the CP optimization can be closely approximated with the ACA optimization as well) at a negative impact on the convergence rate as the number of genes per chromosome is increased from 4 to 11, resulting in a much larger solution space. The y -coordinate of the second baseline thickness control point is fixed at $y = 0.01$ to enforce tangency with baseline thickness.

Table 4 Arbitrary continuous airfoil basic constraints

Constraint	Minimum	Maximum
Camber slope	-0.50	0.50
Camber height (y/c)	-0.10	0.10
Thickness increment slope	-0.50	0.50
Thickness increment (t/c)	0.00	0.15
Baseline thickness (t/c)	0.01	0.01

Table 5 Arbitrary continuous airfoil chromosome buildup

Gene	Parameter
1	Camber cubic Bézier 1 st control point x
2	Camber cubic Bézier 1 st control point y
3	Camber cubic Bézier 2 st control point x
4	Camber cubic Bézier 2 st control point y
5	Thickness increment cubic Bézier 1 st control point x
6	Thickness increment cubic Bézier 1 st control point y
7	Thickness increment cubic Bézier 2 st control point x
8	Thickness increment cubic Bézier 2 st control point y
9	Baseline thickness cubic Bézier 1 st control point x
10	Baseline thickness cubic Bézier 2 st control point y
11	Baseline thickness cubic Bézier 2 st control point x

Double-Edged Plate (DEP)

To evaluate faceted edges against smooth shapes, a double-edged plate is proposed, as shown in Figure 5. Two control points are allowed to vary within constraints. A linear baseline thickness of $t/c = 0.01$ at the x -coordinates of the two control points is added.

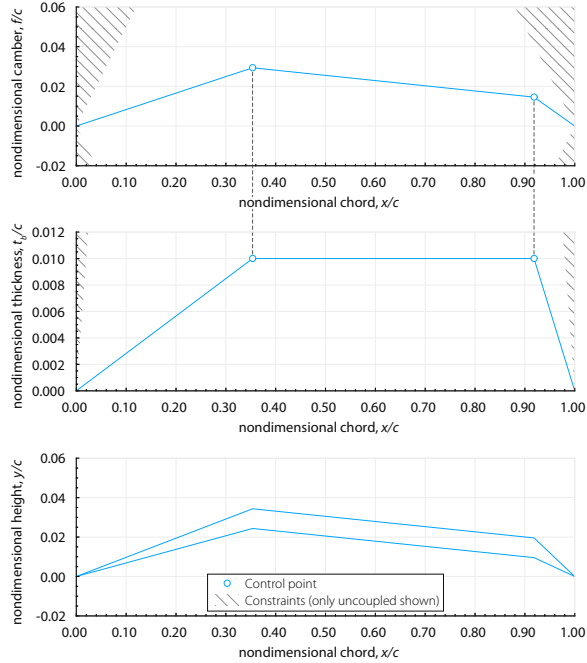


Figure 5 Double-edged plate camber, baseline thickness, and airfoil shape. The vertical axis is enlarged to show details.

To ensure proper gridding, the smallest enclosed angle between two line segments at a control point is constrained to 130 degrees in the present work. The second control point cannot lie on an x -coordinate smaller than the first control point. Table 6 shows the base constraints for the double-edged plate geometry, and Table 7 shows the chromosome buildup.

Table 6 Double-edged plate basic constraints

Constraint	Minimum	Maximum
Camber slope	-0.50	0.50
Camber height (y/c)	-0.10	0.10
Baseline thickness (t/c)	0.01	0.01

Table 7 Double-edged plate chromosome buildup

Gene	Parameter
1	Camber 1 st control point x
2	Camber 1 st control point y
3	Camber 2 st control point x
4	Camber 2 st control point y

Polygonal Airfoil (PAT)

To evaluate the effect of acuity at the leading and trailing edges, the two control points are now allowed to shape an enclosed polygon with the leading edge (LE) and trailing edge (TE) points, as shown in Figure 6. A geometry of interest that lies within this design space is the triangular airfoil, as analyzed by Munday et al.³⁰

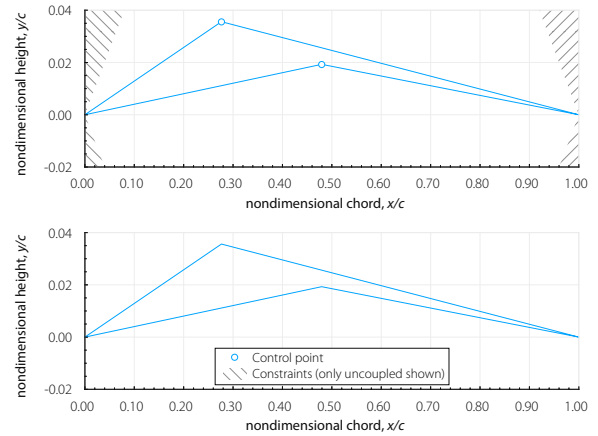


Figure 6 Polygonal airfoil control points and airfoil shape. The vertical axis is enlarged to show details.

The airfoil constraints are performed in such a way that the thickness at the upper surface control point has to be at least $t/c = 0.01$. Furthermore, the enclosed angle at the two control points must be equal or greater than 130 degrees. Table 8 shows the base constraints for the double-edged plate geometry and Table 9 shows the chromosome buildup. The constraints are enforced so that (perturbation) mutations never make airfoil surfaces intersect.

Table 8 Polygonal airfoil basic constraints

Constraint	Minimum	Maximum
Camber slope	-0.50	0.50
Camber height (y/c)	-0.10	0.10
Baseline thickness (t/c)	0.01	0.01

Table 9 Polygonal airfoil chromosome buildup

Gene	Parameter
1	Upper crest 1 st control point x
2	Upper crest 1 st control point y
3	Lower crest 2 st control point x
4	Lower crest 2 st control point y

The double-edged plate and polygonal airfoil both introduce dependent variables (where the cambered plate or arbitrary continuous airfoil had independent variables).

This coupling between GA parameters, or *epistatis*, is where the GA can perform well in optimization if the epistatis is not too high.⁵²

Currently the polygonal shape does not allow for more than four edges and cannot represent corrugated airfoils in particular which might provide superior performance in the low end of the investigated Reynolds number regime.^{9,30,53,54} Future work will include the expansion of the airfoil shapes to include these variations to explore the benefits for the very low Reynolds number range, possibly for the rotor’s inboard geometry.

OBJECTIVE FUNCTION

To be able to perform fitness evaluations, two-dimensional airfoil sections are first analyzed using two-dimensional structured grids and solved using the implicit, compressible Reynolds-Averaged Navier-Stokes (RANS) solver OVERFLOW 2.2o.⁵⁵ Transition modeling is realized using the Spalart-Allmaras (SA) 1-equation turbulence model (SA-neg-1a) with the Coder 2-equation Amplification Factor Transport (AFT) transition model (SA-AFT2017b).⁵⁶ All solutions presented are run time-accurate, in an effort to quantify possible unsteady behavior, and use 6th order central differencing of Euler terms with 2nd order BDF2 time marching.⁵⁵

The function evaluation using a RANS-approach is relatively costly compared to mid-fidelity methods, like XFOIL,⁵⁷ which are only accurate for (mostly) attached flows. The very thick boundary layers at $Re < 10,000$, possibility of substantial flow separation, transient flow features (vortex rollup and vortex shedding), and sharp edges under consideration place this flow outside the domain of simpler panel codes. As the number of function evaluations increases, a RANS approach is still considered a viable solution to explore a solution space of substantial size because the function evaluations are inherently parallel. However, it is important to note that ultimately the cost of repeated fitness function evaluation (i.e. RANS CFD cases) are the prohibitive segment in using this GA for many separate optimizations.

The section lift and drag coefficients are obtained and used in the fitness function evaluations. In case of oscillatory flow in the converged solution, Fourier techniques are used to extract mean values.

Mesh Approach

For all airfoil base types (CP, ACA, DEP, and PAT) the near-body grid is generated using Chimera Grid Tools (CGT) 2.3.⁵⁸ Figure 7 shows a near-body grid example for a CP airfoil type, whereas Figure 8 shows the near-body grid for an airfoil of the PAT type.

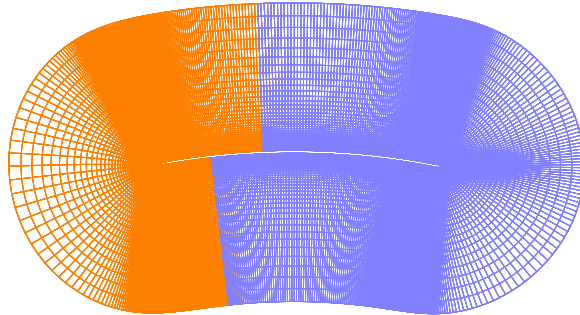


Figure 7 Near body grid for a cambered plate airfoil.

Two body fitted grids model each airfoil (as shown in Figures 7 and 8) and are embedded in a Cartesian background mesh (not shown) that extends 50 chord lengths from the airfoil in all directions. Flow variables are interpolated between grids at the overset boundaries in a manner that preserves the full accuracy of the solver.

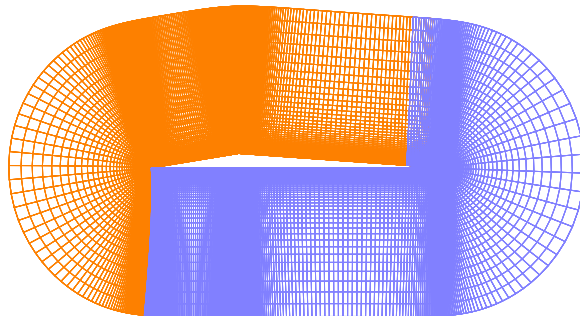


Figure 8 Near body grid for triangular airfoil.

The body fitted grids have a split-O topology which is necessary to accommodate the grid adaption scheme available in OVERFLOW 2.2o. Grid adaption is not pursued in the present work due to the computational cost but it is preserved as an option for further analysis of specific geometries and flow regimes.

The grids place approximately 800 points around the airfoil with the points clustered to ensure geometric fidelity and accurate capture of flow gradients. Grid stretching ratios in all directions do not exceed 10%. The spacing normal to the airfoil surface places the first point at $y^+ < 1$.

Airfoil surfaces are modeled with a viscous boundary condition, and the far field boundaries are modeled using a freestream characteristic boundary condition.

Target Lift Coefficient Modification

It is desirable to have the algorithm optimize at fixed c_l , as fixed angle of attack optimization could yield a c_l that is not practical. Instead of ‘punishing’ the algorithm for an off-target c_l as done by Holst and Pulliam,¹¹ the approach used here is to let the CFD

solver change angle of attack to reach a certain c_l prior to obtaining the performance at that state. As the aerodynamic coefficients at these Reynolds numbers and geometry are generally unsteady, targeting a lift coefficient within a simulation is non-trivial.

The option to attain target c_l values in OVERFLOW was modified to drive $\text{abs}(c_l - c_{l*}) < c_{l,tolerance}$ using alpha. Solution convergence was judged based on the absence of variation from one oscillatory cycle to the next and the steadiness of the mean value for the force and moment coefficients. In preliminary analysis, it was determined that 10,000 timesteps was sufficient to converge the solution on the most challenging configurations and conditions. All CFD solutions for this work ran OVERFLOW with the c_l driver enabled for the first 6,000 timesteps to arrive at an angle of attack that produced the desired lift. The angle of attack was then fixed, and the flow was allowed to continue developing for an additional 4,000 timesteps without perturbation from the c_l driver algorithm. At the end of these 10,000 timesteps, solutions were considered ‘converged’ and mean coefficients were extracted using Fourier techniques. A sample convergence history is shown in Figure 9.

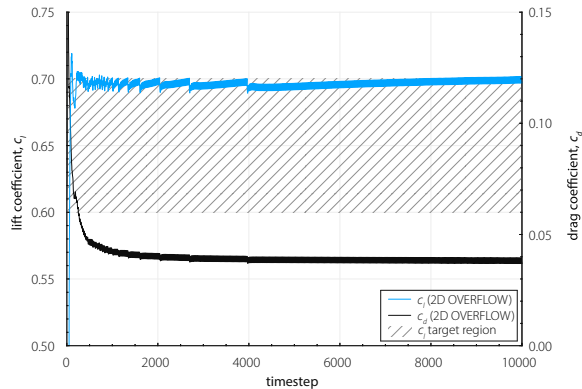


Figure 9 Example performance of airfoil with c_l driver activated.

Fitness Evaluation

The fitness function is the subroutine that assigns the value (or) fitness to a set of variables (section lift and drag in this case). Here it is simply the computation of lift-to-drag ratio at fixed c_l as shown in Eq. 2.

$$F = c_l/c_d, \quad 0.60 \leq c_l \leq 0.70 \quad (2)$$

Flow Conditions

All the optimization simulations are performed for representative Martian atmospheric conditions obtained from Koning et al.²⁹ Table 10 compares the Martian atmosphere to Earth Sea Level Standard (SLS) conditions.

Table 10 Operating conditions for Mars

Variable	Earth SLS	Mars
Density, ρ (kg/m ³)	1.225	0.015 to 0.020
Temperature, T (K)	288.20	248.20 to 193.20
Gas constant, R (m ² /s ² /K)	287.10	188.90
Specific heat ratio, γ	1.400	1.289
Dynamic viscosity, μ (Ns/m ²)	$1.750 \cdot 10^{-5}$	$1.130 \cdot 10^{-5}$
Static pressure, p (kPa)	101.30	0.70 to 0.73

Pleiades Supercomputer

The parallel nature of the GA is used by running all chromosomes of one generation in parallel on the Pleiades supercomputer at NASA Ames Research Center. Each chromosome of a particular generation is assigned its own node and a script keeps track of the progress of each chromosome. Once CFD simulations are completed and cost function values are assigned to each chromosome, the genetic algorithm operators are applied to the chromosomes to create the next generation. The wall clock time for a single generation is around 45 minutes on average.

VALIDATION

The complex unsteady flowfield can be a challenge for RANS methods. Where a grid resolution study would normally be employed, this becomes impractical due to the large number of cases that the algorithm processes. Instead, two representative validation cases are presented for a triangular airfoil and cambered plate airfoil. Error bars presented represent the standard deviation of the integrated forces over the converged timesteps.

TRIANGULAR AIRFOIL

First, a triangular airfoil at $Re = 3,000$ is evaluated at $M = 0.15$ and $M = 0.50$, as reported by Munday et al.³⁰ The airfoil has a maximum thickness of $t/c = 0.05$ and a crest located at $x/c = 0.30$, as shown in Figure 10. Munday et al. analyze the performance of this airfoil using (three dimensional) direct numerical simulations (DNS) and compare with prior experimental studies.

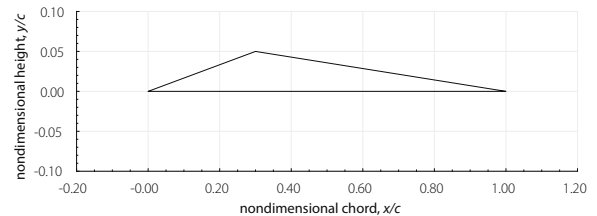


Figure 10 Triangular airfoil as analyzed by Munday et al.³⁰

Figure 11 shows the comparison between the section coefficients from the present study and Munday et al at $Re = 3,000$ and $M = 0.15$.

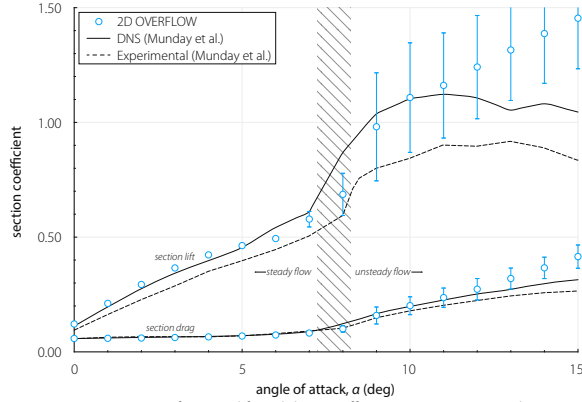


Figure 11 Comparison of section lift and drag coefficients at $Re = 3,000$ and $M = 0.15$ for the triangular airfoil from the present work using OVERFLOW. DNS and experimental results from Munday et al.³⁰

The OVERFLOW results correspond well to the DNS results until, as expected, the stalled angles of attack are reached. Figure 12 shows the comparison at $Re = 3,000$ and $M = 0.50$. At higher Mach number the correlation is good and slightly improved in that it compares well to DNS up to the - now delayed - onset of complete stall. Munday et al. indicate the switch from steady to unsteady flow is delayed with increasing Mach number, which seems to be well captured by OVERFLOW based on the increase in standard deviation from the mean around the same angles of attack. The divergence of the DNS and OVERFLOW simulations is expected at the higher angles of attack, as the OVERFLOW simulations are truly 2D (not allowing three-dimensional structures to develop) and RANS methods' inability to properly predict stall.

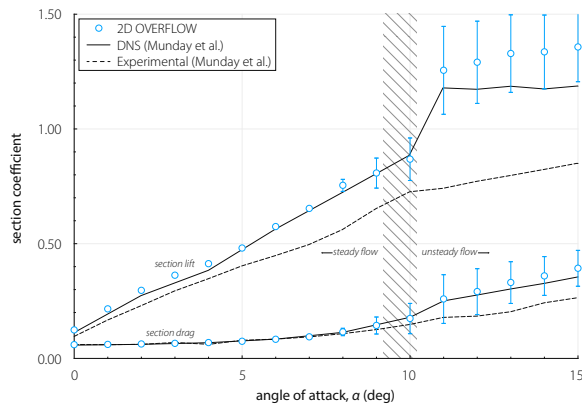


Figure 12 Comparison of section lift and drag coefficients at $Re = 3,000$ and $M = 0.50$ for the triangular airfoil from the present work using OVERFLOW. DNS and experimental results from Munday et al.³⁰

CAMBERED PLATE (5% CIRCULAR ARC)

Koning et al. analyzed the performance of cambered plates and compared the performance of the MHTD using them as direct substitute airfoils.³ Compared to this previous work the present mesh approach and leading-edge shape are changed. The airfoil is shown in Figure 13.

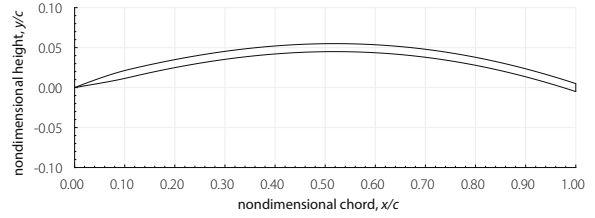


Figure 13 circular arc cambered plate ($f/c = 0.05$, $t/c = 0.01$).

OVERFLOW results are compared to a 5% camber, 1.3% thick plate, as analyzed by Laitone⁵ and a 6% cambered plate with 1% thickness, as analyzed by Okamoto et al.⁹ Figures 14 - 16 show the computed performance compared against the experimental values from Laitone⁵ and Okamoto et al.⁹

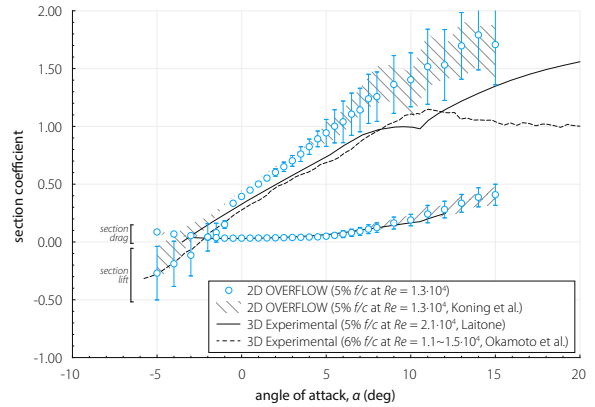


Figure 14 Comparison of section lift and drag coefficients for a $f/c = 5\%$, $t/c = 1\%$ cambered plate using OVERFLOW. Previous OVERFLOW results from Koning et al.³ Experimental results from Laitone⁵ and Okamoto et al.⁹

The earlier results by Koning et al.³ have been included to observe the differences in computational results. Error bars represent the standard deviation of the integrated forces over time.

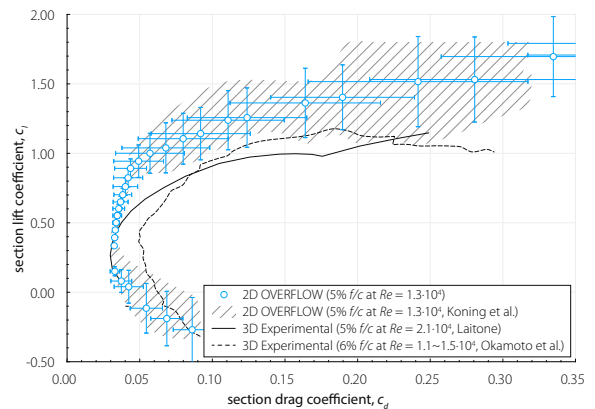


Figure 15 Comparison of section lift and drag coefficients for a 5% f/c , 1% t/c cambered plate using OVERFLOW. Previous OVERFLOW results from Koning et al.³ Experimental results from Laitone⁵ and Okamoto et al.⁹

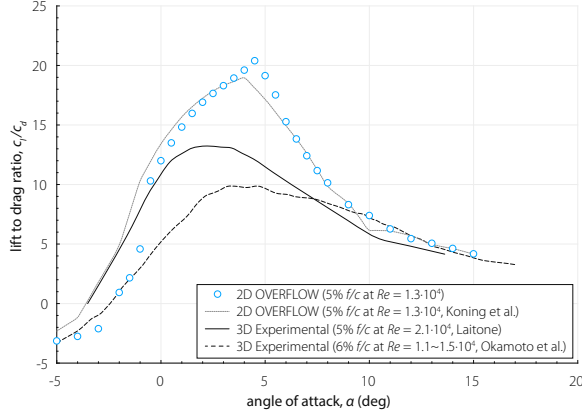


Figure 16 Comparison of section lift-to-drag ratio for a 5% f/c , 1% t/c cambered plate using OVERFLOW. Previous OVERFLOW results from Koning et al.³ Experimental results from Laitone⁵ and Okamoto et al.⁹ (derived).

The angles of attack during negative stall (around $\alpha < -2^\circ$) match better with experimental data, but the lift is overpredicted. The exact leading edge shape of the experiments, however, is not equal, nor is the exact overall geometry and conditions. The results show a good comparison of the minimum drag coefficient, but the simulations show higher performance compared to the experimental work.

Experimental testing of airfoils at low Reynolds numbers is difficult due to thick boundary layers in tunnel test sections (or on splitter plates),³⁰ the low forces (and thus sensitive equipment needed),⁵ and the possible increased influence of external factors on laminar-turbulent transition (near the critical Reynolds number).^{31,59} These difficulties add to uncertainty regarding tunnel test results at very low Reynolds numbers.

RESULTS

The algorithm is tasked to optimize airfoils at two conditions as outlined in Table 11. Conditions 1 and 2 are considered representative for a Martian rotor at $r/R = 0.50$, and $r/R = 0.75$, respectively.

Table 11 Conditions for optimization cases

Parameter	Condition 1	Condition 2
Mach	0.35	0.50
Reynolds number	11,352	16,682
Target c_l	0.65	0.65

Figure 17 shows the relatively rapid convergence for condition 2 using the PAT airfoil type (4 genes per chromosome). The case can be seen to converge around generation 20. Figure 18 shows the relatively slow convergence for condition 1 using the ACA airfoil type (11 genes per chromosome). Convergence for the ACA airfoil type is seen at a later generation due to the increase in the solution space size attributed to the increase in number of genes per chromosome. This leads

to a substantial increase in function evaluations required prior to convergence.

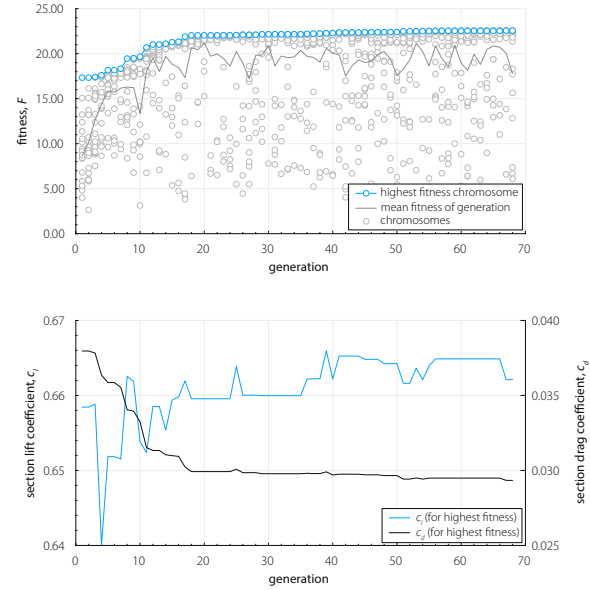


Figure 17 Convergence for PAT optimization at $Re = 16,682$, $M = 0.50$, and $c_l^* = 0.65$.

To compare the performance of the obtained airfoils, baseline performance is obtained by modeling the *clf5605* airfoil from the MHTD (outboard 50% of the blade), as reported in Koning et al.¹⁴ and the 5% cambered plate airfoil, as shown in Figure 13. From those baselines, the relative improvements obtained by the optimization are deduced. Table 12 shows the performance of the optimized airfoils at condition 1. Table 13 shows the resulting camber and thickness maxima for the optimized airfoils at condition 1.

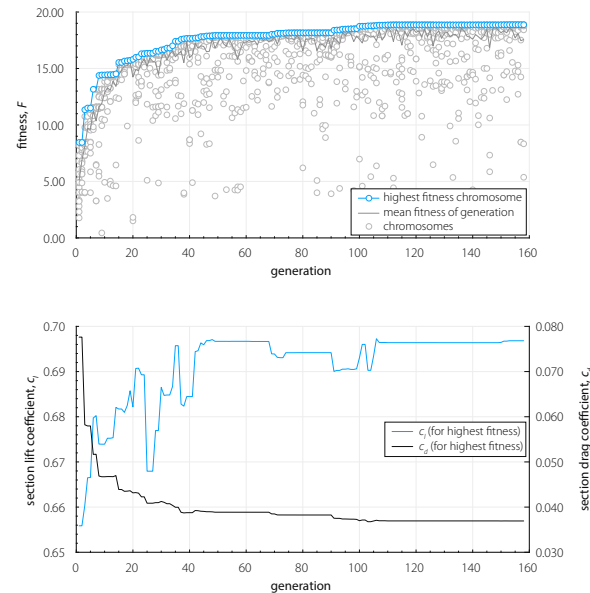


Figure 18 Convergence for ACA optimization at $Re = 11,354$, $M = 0.35$, and $c_l^* = 0.65$.

Table 12 Optimization results for condition 1: $Re = 11,354$, $M = 0.35$, and $c_r = 0.65$

Airfoil	Generation	Fitness (c_l/c_d)	Improvement
clf5605	N/A	16.47	0.00%
5% cambered plate	N/A	17.72	7.59%
CP	70	19.09	15.91%
ACA	180	18.87	14.57%
DEP	55	18.89	14.69%
PAT	82	18.72	13.66%

Table 13 Optimized geometry for condition 1: $Re = 11,354$, $M = 0.35$, and $c_r = 0.65$

Airfoil	Camber (f/c)	Thickness (t/c)
clf5605	0.050	0.050
5% cambered plate	0.050	0.010
CP	0.028	0.010
ACA	0.034	0.018
DEP	0.035	0.010
PAT	0.019	0.021

It can be seen that for remarkably different airfoil types (especially differences in faceted features versus smooth shapes), the fitness scores are close to each other but show substantial increases in efficiency compared to the reference airfoils. Table 14 shows the performance of the optimized airfoils at condition 2. Table 15 shows the resulting camber and thickness maxima for the optimized airfoils at condition 2.

Table 14 Optimization results for condition 2: $Re = 16,682$, $M = 0.50$, and $c_r = 0.65$

Airfoil	Generation	Fitness (c_l/c_d)	Improvement
clf5605	N/A	18.34	0.00%
5% cambered plate	N/A	20.51	11.83%
CP	70	23.70	29.22%
ACA	170 [†]	21.46	17.01%
DEP	69	23.43	27.75%
PAT	68	22.57	23.06%

The flow fields in the near-body mesh for the optimized airfoils in condition 2 are shown in Figures 19 - 22 for the CP, ACA, DEP, and PAT airfoil optimizations, respectively.

Table 15 Optimized geometry for condition 2: $Re = 16,682$, $M = 0.50$, and $c_r = 0.65$

Airfoil	Camber (f/c)	Thickness (t/c)
clf5605	0.050	0.050
5% cambered plate	0.050	0.010
CP	0.031	0.010
ACA	0.022	0.039
DEP	0.029	0.010
PAT	0.023	0.028

All optimized airfoils are observed to shed coherent vortices, likely indicating that these contribute positively to the performance of the airfoil.

The CP and DEP airfoils are further evaluated at $M = 0.50$, $M = 0.70$, and $M = 0.90$ to evaluate the high Mach performance of these airfoils and are compared to the performance of the reference airfoils. The Reynolds number is scaled with Mach number.

[†] The ACA case is not fully converged, but was not continued due to the large number of generations required.

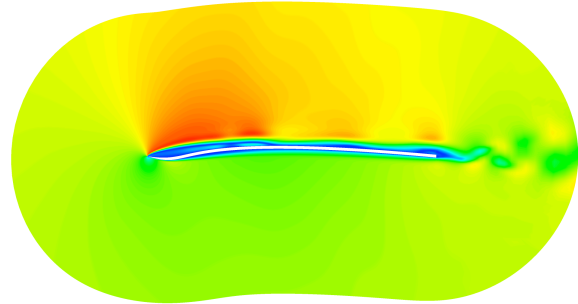


Figure 19 Converged CP optimization flowfield, condition 2, velocity magnitude.

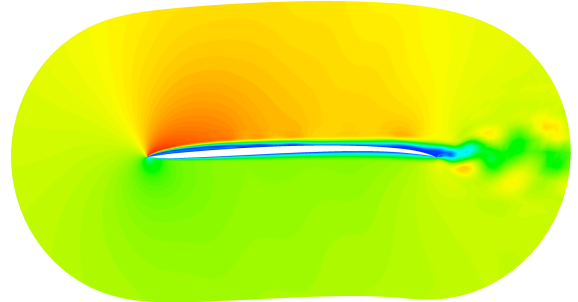


Figure 20 Converged ACA optimization flowfield, condition 2, velocity magnitude.

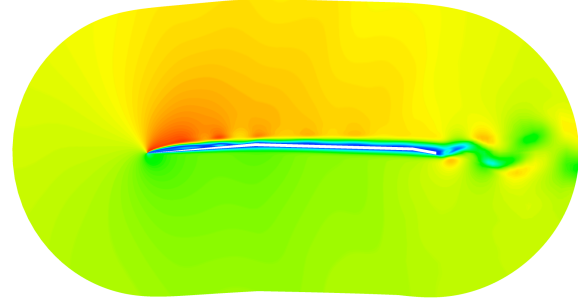


Figure 21 Converged DEP optimization flowfield, condition 2, velocity magnitude.

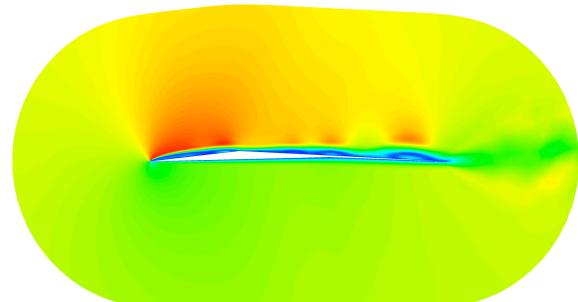


Figure 22 Converged PAT optimization flowfield, condition 2, velocity magnitude.

Figure 23 shows the lift-drag polar and the lift-to-drag ratio versus angle of attack for the three airfoils. The optimal lift-to-drag ratio occurs, as expected, at the design lift coefficient. Both optimized airfoils have a higher peak lift-to-drag ratio, but the clf5605 out-

performs the optimized airfoils at lift coefficients exceeding the target lift coefficient.

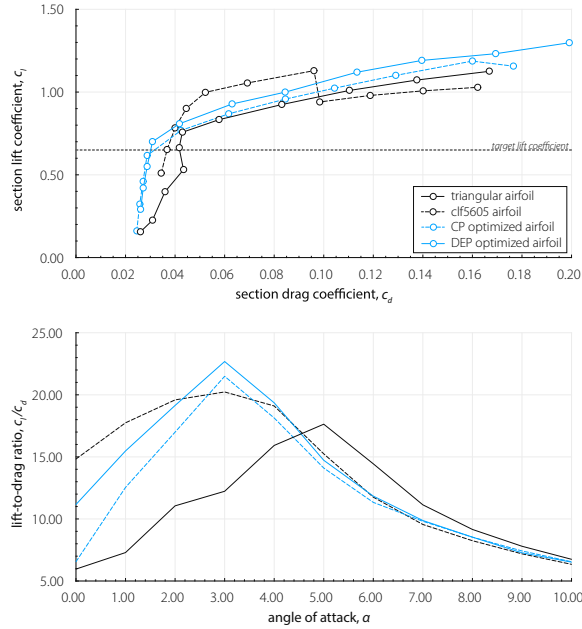


Figure 23 CP and DEP optimized airfoils at $c_r = 0.65$, versus clf5605 at $M = 0.50$.

The jump in performance for the clf5605 airfoil occurs due to a simulated flow state change from vortex rollup to leading edge separation.²⁹ Figure 24 shows the same plot, but for $M = 0.70$ and $Re = 23,607$. The advantage of the clf5605 airfoils at lift coefficients exceeding the target lift coefficient has now disappeared, primarily due to local supersonic flow on the airfoil. Both optimized airfoils have an increased peak lift-to-drag ratio.

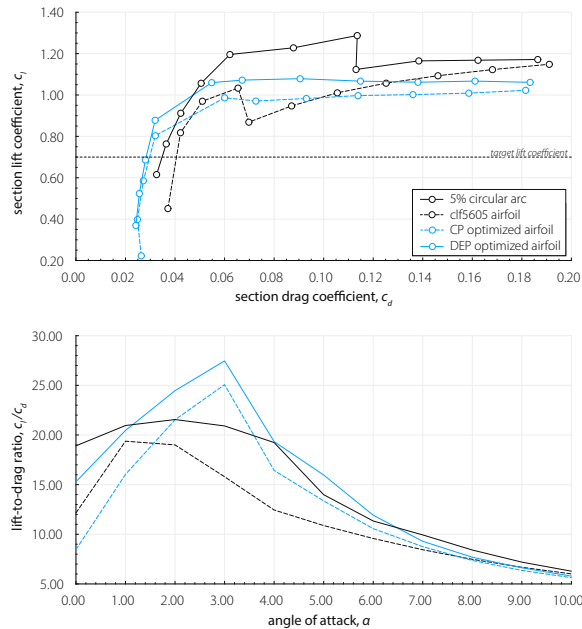


Figure 24 CP and DEP optimized airfoils at $c_r = 0.65$, versus clf5605 at $M = 0.70$.

Figure 25 shows the same plot, but for $M = 0.90$. The performance of all airfoils is reduced significantly, but the relative advantage of the DEP optimized airfoil is evident, as its lift-to-drag ratio and lift-drag polar are out-performing the other airfoils over the entire angle of attack range.

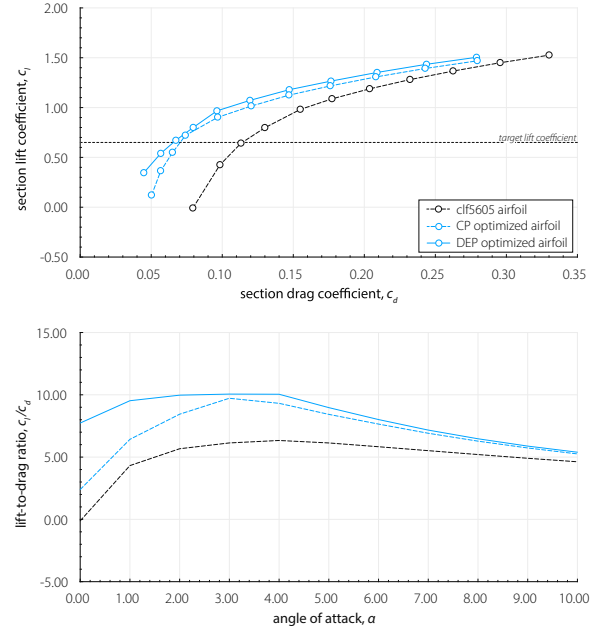


Figure 25 CP and DEP optimized airfoils at $c_r = 0.65$, versus clf5605 at $M = 0.90$.

Figures 26 - 28 show the Mach plots for the clf5605, CP optimized airfoil, and DEP optimized airfoil at $\alpha = 3^\circ$, $M = 0.90$ and $Re = 30,351$. The shockwaves at the upper and lower surfaces are visible. The DEP optimized airfoil shows a relatively weak frontal shockwave when compared with the CP optimized airfoil.

The algorithm was not used to optimize performance at very high subsonic Mach numbers at this point. Further compressible analyses may benefit from Adaptive Mesh Refinement (AMR)⁶⁰ to resolve the shocks more accurately.

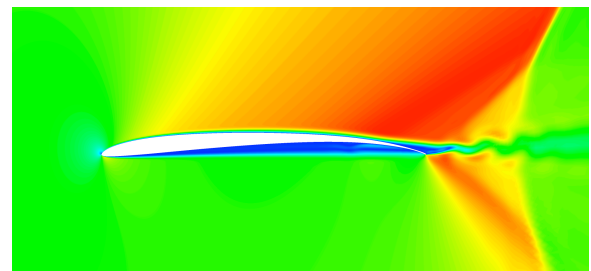


Figure 26 Mach plot for clf5605 at $\alpha = 3^\circ$, $M = 0.90$ showing shockwaves.

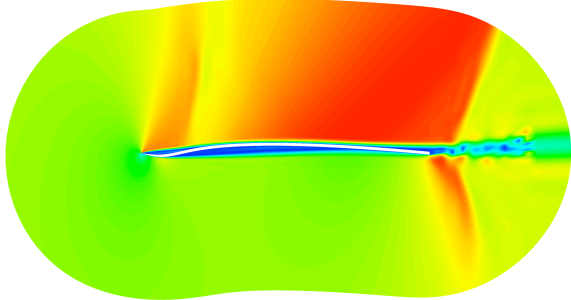


Figure 27 Mach plot for CP optimized airfoil at $\alpha = 3, M = 0.90$ showing shockwaves.

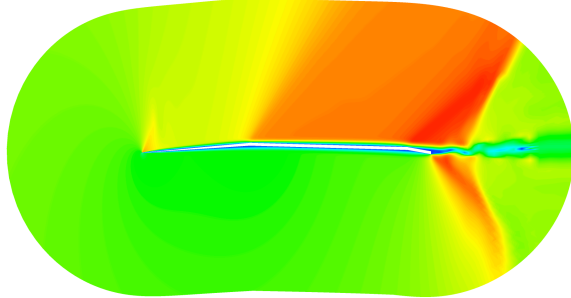


Figure 28 Mach plot for DEP optimized airfoil at $\alpha = 3, M = 0.90$ showing shockwaves.

CONCLUSIONS

Airfoils are optimized for maximum lift-to-drag ratio in the Martian atmosphere at a target lift coefficient, $c_{l*} = 0.65$. Two representative flight conditions for rotor operation in the Martian atmosphere are investigated at $M = 0.35, Re = 11,352$ and $M = 0.50, Re = 16,682$, condition 1 and 2 respectively. The genetic algorithm produced airfoils with an increase in lift-to-drag ratio of approximately 16% to 29%, compared to the clf5605 airfoil of the MHTD.

Comparison of the drag polar at $M = 0.50$ for the CP and DEP optimized airfoils shows the clf5605 airfoil obtains higher lift coefficients for lower drag when exceeding the target lift coefficient. Increasing the Mach number to $M = 0.70$ and $M = 0.90$ favors both the CP and DEP airfoils, with the DEP airfoils ultimately showing the highest performance at $M = 0.90$.

The high performance of the DEP optimized airfoil could be due to the same mechanics as described in Munday et al.³⁰ for the triangular airfoil. Both the DEP optimized airfoil and the triangular airfoil have local faceting. Munday et al. describe a ‘critical angle of attack’ at which the separation moves from the upper surface crest to the leading edge, providing a nonlinear (or bilinear) lift curve. They conclude that compressibility increases this angle of attack, which could explain the relatively good performance of the DEP optimized airfoil at high Mach numbers.

A rotor performance model should be generated (once an optimized airfoil is fully refined) to observe differences in performance with published results for the MHTD. The rotor performance model by Koning et al. estimates the MHTD rotor profile power to be between 25% and 33% of the total power in the design thrust coefficient range.²⁹ Reducing the profile power between 16% and 29% as by the current work could yield improvements in figure of merit of around 4% to 10% for the MHTD in hover.

FUTURE WORK

The genetic algorithm can be improved with adaptative parameter control and local (gradient-based) optimizers near local optima.⁵¹ Despite the increase in algorithm complexity, this could yield much faster evaluation of local minima or maxima.

Although the current single objective optimization (SOO) is promising, to further investigate these airfoils, multi objective optimization (MOO) is necessary. Doing so would allow further airfoil analysis between drag minimization, lift maximization, and attainable Mach numbers near the blade tip.

Currently, the polygonal shapes do not allow for ‘higher order’, arbitrary polygonal airfoils or corrugated airfoils that might provide superior performance in the low end of the investigated Reynolds number regime. Future work will include the expansion of the airfoil shapes to include these variations to explore the benefits for the very low Reynolds number range, possibly for the inboard rotor geometry.

The airfoil performance needs to be further investigated with analysis of the transient pressure distribution on the airfoils, the origin of the coherent vortices, and their contribution to airfoil performance.

ACKNOWLEDGEMENTS

The authors would like to thank Larry Young and Alan Wadcock for their insightful discussions. Geoffrey Ament, Haley Cummings, Jessica Deming, Showvik Haque, Kristen Kallstrom, and Natalia Perez Perez, are thanked for reviewing this document and their helpful suggestions. Elisa Sauron is thanked for her kind support. The support from William Warmbrodt and Larry Hogle during this research is greatly appreciated.

BIBLIOGRAPHY

- 1 Balaram, J. (Bob), Daubar, I. J., Bapst, J., and Tzanetos, T., "Helicopter on Mars: Compelling Science of Extreme Terrains Enabled by an Aerial Platform," *9th International Conference on Mars*, Pasadena, California: 2019.
- 2 Tzanetos, T., "Mars Science Helicopter" Available: <https://www-robotics.jpl.nasa.gov/tasks/showTask.cfm?FuseAction=ShowTask&TaskID=353&tdaID=700145>.
- 3 Koning, W. J. F., Romander, E. A., and Johnson, W., "Low Reynolds Number Airfoil Evaluation for the Mars Helicopter Rotor," *AHS International 74th Annual Forum & Technology Display*, Phoenix, Arizona: 2018.
- 4 Schmitz, F. W., *Aerodynamics of the model airplane. Part 1 - Airfoil measurements*, Huntsville, Alabama: 1967.
- 5 Laitone, E. V., "Wind tunnel tests of wings at Reynolds numbers below 70 000," *Experiments in Fluids*, vol. 23, Nov. 1997, pp. 405–409.
- 6 McMasters, J., and Henderson, M., "Low-speed single-element airfoil synthesis," *Technical Soaring*, vol. 6, 1980, pp. 1–21.
- 7 Carmichael, B. H., *Low Reynolds Number Airfoil Survey, Volume 1*, Capistrano Beach, California: 1981.
- 8 Wazzan, A. R., Okamura, T. T., and Smith, A. M. O., *Spatial and Temporal Stability Charts for the Falkner-Skan Boundary-Layer Profiles*, 1968.
- 9 Okamoto, M., Yasuda, K., and Azuma, A., "Aerodynamic characteristics of the wings and body of a dragonfly," *The Journal of Experimental Biology*, vol. 199, Feb. 1996, pp. 281 LP – 294.
- 10 Koning, W. J. F., *Airfoil Selection for Mars Rotor Applications*, Moffett Field, California, NASA CR-2019-220236: 2019.
- 11 Holst, T., and Pulliam, T., "Aerodynamic shape optimization using a real-number-encoded genetic algorithm," *19th AIAA Applied Aerodynamics Conference*, 2001, p. 2473.
- 12 Sampaio, L. E. B., Rezende, A. L. T., and Nieceke, A. O., "The challenging case of the turbulent flow around a thin plate wind deflector, and its numerical prediction by LES and RANS models," *Journal of Wind Engineering and Industrial Aerodynamics*, vol. 133, 2014, pp. 52–64.
- 13 Rezende, A. L. T., and Nieceke, A. O., "Evaluation Of Turbulence Models To Predict The Edge Separation Bubble Over A Thin Aerofoil," *Proceedings of the 20th International Congress of Mechanical Engineering-COBEM*, 2009.
- 14 Koning, W. J. F., Johnson, W., and Allan, B. G., "Generation of Mars Helicopter Rotor Model for Comprehensive Analyses," *AHS Aeromechanics Design for Transformative Vertical Flight*, San Francisco, California: 2018.
- 15 Kroo, I., Prinz, F., Shantz, M., Kunz, P., Fay, G., Cheng, S., Fabian, T., and Partridge, C., "The Mesicopter: A Miniature Rotorcraft Concept Phase II Interim Report," *Stanford university*, 2000.
- 16 Kunz, P. J., and Kroo, I., "Analysis and Design of Airfoils For Use at Ultra-Low Reynolds Numbers," *fixed and flapping wing aerodynamics for micro air vehicle applications*, vol. 195, 2001, pp. 35–59.
- 17 Oyama, A., and Fujii, K., "A study on airfoil design for future Mars airplane," *44th AIAA Aerospace Sciences Meeting and Exhibit*, 2006, p. 1484.
- 18 Anyoji, M., Nose, K., Ida, S., Numata, D., Nagai, H., and Asai, K., "Low Reynolds number airfoil testing in a Mars wind tunnel," *40th Fluid Dynamics Conference and Exhibit*, 2010, p. 4627.
- 19 Anyoji, M., Nonomura, T., Aono, H., Oyama, A., Fujii, K., Nagai, H., and Asai, K., "Computational and experimental analysis of a high-performance airfoil under low-Reynolds-number flow condition," *Journal of Aircraft*, vol. 51, 2014, pp. 1864–1872.
- 20 Anyoji, M., Numata, D., Nagai, H., and Asai, K., "Effects of Mach Number and Specific Heat Ratio on Low-Reynolds-Number Airfoil Flows," *AIAA Journal*, vol. 53, Oct. 2014, pp. 1640–1654.
- 21 Winslow, J., Otsuka, H., Govindarajan, B., and Chopra, I., "Basic Understanding of Airfoil Characteristics at Low Reynolds Numbers," *7th AHS Technical Meeting on VTOL Unmanned Aircraft Systems*, Mesa, AZ: 2017.
- 22 Srinath, D. N., and Mittal, S., "Optimal aerodynamic design of airfoils in unsteady viscous flows," *Computer Methods in Applied Mechanics and Engineering*, vol. 199, 2010, pp. 1976–1991.
- 23 Desert, T., Moschetta, J.-M., and Bezard, H., "Numerical and experimental investigation of an airfoil design for a Martian micro rotorcraft," *International Journal of Micro Air Vehicles*, vol. 10, 2018, pp. 262–272.
- 24 "NASA's Mars Helicopter Completes Flight Tests" Available: <https://www.jpl.nasa.gov/news/news.php?feature=7361>.
- 25 Balaram, J. (Bob), Canham, T., Duncan, C., Golombek, M., Grip, H. F., Johnson, W., Maki, J., Quon, A., Stern, R., and Zhu, D., "Mars Helicopter Technology Demonstrator," *AIAA Science and Technology Forum and Exposition (AIAA SciTech)*, 2018.
- 26 Grip, H. F., Johnson, W., Malpica, C., Scharf, D. P., Mandić, M., Young, L., Allan, B., Mettler, B., and Martin, M. S., "Flight Dynamics of a Mars Helicopter," *43rd European Rotorcraft Forum*, 2017.
- 27 Grip, H. F., Scharf, D. P., Malpica, C., Johnson, W., Mandic, M., Singh, G., and Young, L. A., "Guidance and control for a Mars helicopter," *2018 AIAA Guidance, Navigation, and Control Conference*, 2018, p. 1849.

- 28 Pipenberg, B. T., Keennon, M., Tyler, J., Hibbs, B.,
Langberg, S., Balaram, J., Grip, H. F., and
Pempejian, J., "Design and Fabrication of the Mars
Helicopter Rotor, Airframe, and Landing Gear
Systems," *AIAA Scitech 2019 Forum*, 2019, p. 620.
- 29 Koning, W. J. F., Johnson, W., and Grip, H. F.,
"Improved Mars helicopter aerodynamic rotor model
for comprehensive analyses," *AIAA Journal*, 2019,
pp. 1–10.
- 30 Munday, P. M., Taira, K., Suwa, T., Numata, D.,
and Asai, K., "Nonlinear lift on a triangular airfoil in
low-Reynolds-number compressible flow," *Journal of
Aircraft*, vol. 52, 2014, pp. 924–931.
- 31 Van Ingen, J., "The eN method for transition
prediction. Historical review of work at TU Delft,"
38th Fluid Dynamics Conference and Exhibit, 2008,
p. 3830.
- 32 Saric, W. S., Reed, H. L., and Kerschen, E. J.,
"Boundary-layer receptivity to freestream
disturbances," *Annual review of fluid mechanics*, vol.
34, 2002, pp. 291–319.
- 33 Hoerner, S. F., *Fluid-Dynamic Drag: Practical
Information on Aerodynamic Drag and
Hydrodynamic Resistance*, Hoerner Fluid Dynamics,
1965.
- 34 McArthur, J., *Aerodynamics of wings at low
Reynolds numbers: boundary layer separation and
reattachment*, University of Southern California,
2008.
- 35 Winslow, J., Otsuka, H., Govindarajan, B., and
Chopra, I., "Basic Understanding of Airfoil
Characteristics at Low Reynolds Numbers (104–
105)," *Journal of Aircraft*, Dec. 2017, pp. 1–12.
- 36 Werlé, H., *Le tunnel hydrodynamique au service de
la recherche aérospatiale*, Office National d'Études et
de Recherches Aérospatiales, 1974.
- 37 Van Dyke, M., and Van Dyke, M., "An album of fluid
motion," 1982.
- 38 Boiko, A. V., Grek, G. R., Dovgal, A. V., and Kozlov,
V. V., *The origin of turbulence in near-wall flows*,
Springer Science & Business Media, 2013.
- 39 Alam, M. M., Zhou, Y., Yang, H. X., Guo, H., and
Mi, J., "The ultra-low Reynolds number airfoil wake,"
Experiments in fluids, vol. 48, 2010, pp. 81–103.
- 40 Pauley, L. L., Moin, P., and Reynolds, W. C., "The
structure of two-dimensional separation," *Journal of
Fluid Mechanics*, vol. 220, 1990, pp. 397–411.
- 41 Holland, J. H., "Genetic algorithms," *Scientific
american*, vol. 267, 1992, pp. 66–73.
- 42 Holland, J. H., and Goldberg, D., "Genetic
algorithms in search, optimization and machine
learning," *Massachusetts: Addison-Wesley*, 1989.
- 43 Grasmeyer, J., and Grasmeyer, J., "Application of a
genetic algorithm with adaptive penalty functions to
airfoil design," *35th Aerospace Sciences Meeting and
Exhibit*, 1997, p. 7.
- 44 Jones, B. R., Crossley, W. A., and Lyrantzis, A. S.,
"Aerodynamic and aeroacoustic optimization of
rotorcraft airfoils via a parallel genetic algorithm,"
Journal of Aircraft, vol. 37, 2000, pp. 1088–1096.
- 45 Yamamoto, K., and Inoue, O., "Applications of
genetic algorithm to aerodynamic shape
optimization," *12th Computational Fluid Dynamics
Conference*, 1995, p. 1650.
- 46 Pulliam, T., Nemec, M., Holst, T., and Zingg, D.,
"Comparison of evolutionary (genetic) algorithm and
adjoint methods for multi-objective viscous airfoil
optimizations," *41st Aerospace Sciences Meeting and
Exhibit*, 2003, p. 298.
- 47 Sobieczky, H., "Geometry generator for CFD and
applied aerodynamics," *New Design Concepts for
High Speed Air Transport*, Springer, 1997, pp. 137–
157.
- 48 Sobieczky, H., "Parametric airfoils and wings,"
*Recent development of aerodynamic design
methodologies*, Springer, 1999, pp. 71–87.
- 49 Shahrokhi, A., and Jahangirian, A., "Airfoil shape
parameterization for optimum Navier–Stokes design
with genetic algorithm," *Aerospace science and
technology*, vol. 11, 2007, pp. 443–450.
- 50 Stone, M. C., and DeRose, T. D., "A geometric
characterization of parametric cubic curves," *ACM
Transactions on Graphics (TOG)*, vol. 8, 1989, pp.
147–163.
- 51 Goldapp, M., "Approximation of circular arcs by
cubic polynomials," *Computer Aided Geometric
Design*, vol. 8, 1991, pp. 227–238.
- 52 Haupt, R. L., and Ellen Haupt, S., "Practical genetic
algorithms," 2004.
- 53 Kesel, A. B., "Aerodynamic characteristics of
dragonfly wing sections compared with technical
aerofoils," *Journal of Experimental Biology*, vol. 203,
2000, pp. 3125–3135.
- 54 Levy, D.-E., and Seifert, A., "Simplified dragonfly
airfoil aerodynamics at Reynolds numbers below
8000," *Physics of Fluids*, vol. 21, 2009, p. 71901.
- 55 Pulliam, T., "High order accurate finite-difference
methods: as seen in OVERFLOW," *20th AIAA
Computational Fluid Dynamics Conference*, 2011, p.
3851.
- 56 Coder, J. G., and Maughmer, M. D., "Computational
fluid dynamics compatible transition modeling using
an amplification factor transport equation," *AIAA
Journal*, vol. 52, 2014, pp. 2506–2512.
- 57 Drela, M., "XFOIL: An Analysis and Design System
for Low Reynolds Number Airfoils," *Low-Reynolds
Number Aerodynamics*, 1989.
- 58 Chan, W. M., Rogers, S. E., Nash, S. M., Buning, P.
G., Meakin, R. L., Boger, D. A., and Pandya, S.,
"Chimera Grid Tools User's Manual, Version 2.0,"
NASA Ames Research Center, 2007.
- 59 Wang, S., Zhou, Y., Alam, M. M., and Yang, H.,
"Turbulent intensity and Reynolds number effects on
an airfoil at low Reynolds numbers," *Physics of
Fluids*, vol. 26, 2014, p. 115107.
- 60 Buning, P. G., and Pulliam, T. H., "Near-body grid
adaption for overset grids," *46th AIAA Fluid
Dynamics Conference*, 2016, p. 3326.